Influence of Wing Shapes on Surface Pressure Fluctuations at Wing-Body Junctions

Semih M. Ölçmen* and Roger L. Simpson†

Virginia Polytechnic Institute and State University, Blacksburg, Virginia 24061

The body surface pressure fluctuations along the stagnation streamlines of several wing-body junctions were measured with microphones. The wing shapes are of a 3:2 semielliptical-nosed NACA-0020-tailed body, a parallel centerbody model, a tear drop shape, Sand 1850, NACA-0015, and NACA-0012. The oil-flow visualizations revealed the limiting streamline structure on the wall where the models were mounted. Measurements were conducted at a nominal reference velocity of 32.5 m/s and Reynolds number based on approach momentum thickness of 4450. Pressure-fluctuation measurements at the nose region show the existence of the bimodal pressure-fluctuation histograms and oil-flow visualization pictures show the primary separation regions, line of low shear, and the fish-tail-shaped wake region. The measurements show that the pressure fluctuations and the primary separation line location at the nose highly differ depending on the nose geometry. The histograms of the pressure-fluctuation data show that the fluctuations are different than Gaussian. A simple physical relationship between the pressure fluctuations and the body geometry is given.

Nomenclature

c	= chord length
D	= distance of the line of low shear and the first separation line merge measured from the leading edge of the wing
f	= frequency
L	= distance of the separation of the flow near the trailing edge from the leading edge of the wing
p	= pressure fluctuation
$P(p)$	= probability density function
PU	= pressure force/U momentum
PV	= pressure force/V momentum
p_{rms}	= square root of the averaged pressure fluctuations
q_{ref}	= reference dynamic pressure
R	= leading-edge radius
Re_θ	= Reynolds number based on momentum thickness
S	= sensitivity
t	= maximum thickness of a given wing
U	= streamwise velocity component
U_{ref}	= reference velocity
u	= u component of the fluctuating velocity
W	= wake width
W_{max}	= maximum width of the horseshoe vortex zone
X_{sep}	= primary separation distance from the leading edge of the wing
X_{lols}	= distance of the line of low shear from the leading edge of the wing
x, y, z	= Cartesian coordinate system axes
δ	= boundary-layer thickness
θ	= momentum thickness, and an angle
δ^*	= displacement thickness
Δp	= increment in pressure fluctuations
$\Delta \omega$	= bandwidth of ω
$\phi(\omega)$	= autospectral density function
ω	= $2\pi f$, rad/s

I. Introduction

IN the presence of a wing protruding from a surface, the vorticity in the approach boundary layer forming on the surface rolls up and stretches around the wing to form a vortex pattern resembling a horseshoe. The flow pattern at the nose region and around the wing close to the surface is highly dominated by this vortex.[1] The strength and the rate of stretching of the vortex depends highly on the wing shape, since the mean pressure gradients affecting the flowfield are determined with the wing shape.[1,2] The structure of the vortex at the nose appears to be highly unsteady.[3] While the "horseshoe vortex" nearest the wing nose is being stretched, newer younger vortices are formed upstream.[4] The younger vortices grow with time while the oldest vortex is reduced in size by stretching.[4] Eventually one or more of these new vortices merge with what is left of the oldest one to form another "old" vortex nearest the nose.[4] The process is then repeated, although the process is never periodic.[3,4] The rolling up of the unsteady vortices directs the high-momentum freestream flow towards the surface at the nose region, which causes high-pressure fluctuations in this region. Thus, pressure fluctuations caused by the flowfield are also not periodic. The histograms of the pressure fluctuations show two distinct peaks (bimodal) for some wing shapes, which mean that the fluctuations are likely to occur at two distinct and separate ranges.

In this study, the high-pressure fluctuations at the nose section of a wing due to the unsteady horseshoe vortex formation is studied (Fig. 1). The pressure-fluctuation data are used to investigate the characteristics of the pressure fluctuations and to find the locations of the bimodal flow structure forming ahead of the body. In applications, this bimodal flow structure and flow-induced vibrations of the solid wing/body structure can generate unwanted low-frequency noise which is carried around and away from the wing.[3]

The techniques used in this investigation include microphones for the measurement of the pressure fluctuations, hot-wire anemometry for the measurement of the velocity profiles to define the incoming boundary layers, and the oil-flow technique to visualize the limiting streamline structure on the wall. First the description of the models, the techniques used to obtain and extract the data, the general description of the tunnel, and the flow conditions will be given. Next the results will be discussed.

Here we examine the surface pressure-fluctuation behavior in the plane of mean flow symmetry for several symmetric airfoils or struts.

II. Experimental Apparatus and Techniques

A. Description of the Tunnel and Flow Conditions

The measurements were carried out in the boundary-layer tunnel at Virginia Polytechnic Institute and State University. The tunnel used was the same as described by Devenport and Simpson.[3] The length of the tunnel test section is 8 m. The measurements were planned for a Reynolds number based on momentum thickness of ≈ 4500. To achieve this goal in this tunnel, a false floor was used. The boundary layer formed on the tunnel floor starting at the tunnel entrance was sucked out through a scoop which was at 1.73 m away from the entrance to start the formation of a new boundary layer on the false floor. This resulted in approximately 1.18 m between the scoop and the leading edge of the wing for the development of the new boundary layer. The mean static pressure throughout the tunnel on the false floor was kept constant with use of a trailing-edge flap which was sitting at a 7-deg angle with respect to the floor.

The measurements were made at a nominal speed of 32.5 m/s. The approach boundary layer was measured with a hot-wire anemometer at 0.655 m ahead of the 3:2 elliptical-nosed NACA-0020-tailed body in the presence of the body ($\theta = 2.194$ mm, $\delta = 18.74$ mm, and $\delta^* = 3.049$ mm). The turbulence intensity of the tunnel at 27 m/s was 0.1% and the potential core was uniform within 0.5% in the spanwise and 1% in the vertical directions, respectively. The Reynolds number based on momentum thickness was $Re_\theta = 4450$.
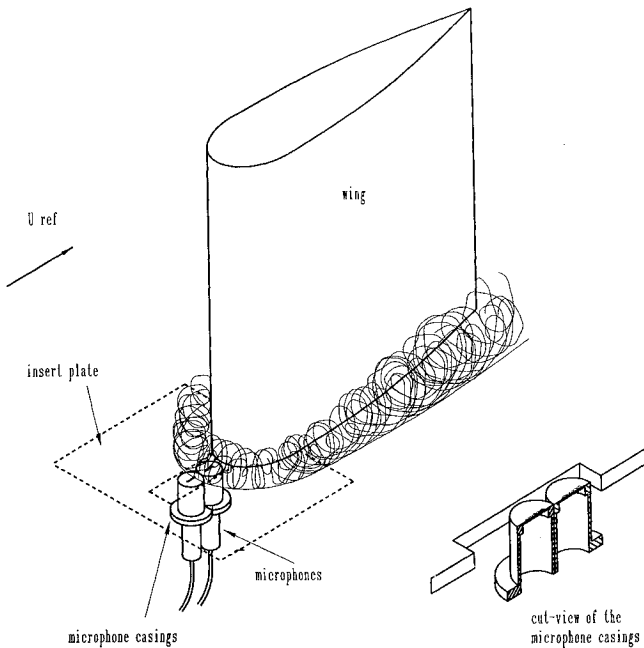
B. Wing Shapes

The wing shapes used in the investigation were 3:2 semielliptical-nosed NACA-0020-tailed wing, a parallel centerbody model, a tear drop shape, Sand 1850, NACA-0015, and NACA-0012. The important characteristics of each wing and how they are numbered is given in Table 1. Each model had a height of 22.9 cm. Figure 2 shows the body shapes traced around the models used. Each model was tripped with 120 grade sandpaper to ensure that the boundary layers formed on the wings were turbulent. Each model was held such that the leading edges of each model would be at the same point where model 0 (3:2 semielliptical-nosed NACA-0020-tailed wing) was held. This was done to make the incoming boundary layer the same for each model.

The shapes of the NACA profiles may be found in Abbott and von Doenhoff.[5] The tear drop body had a circular nose
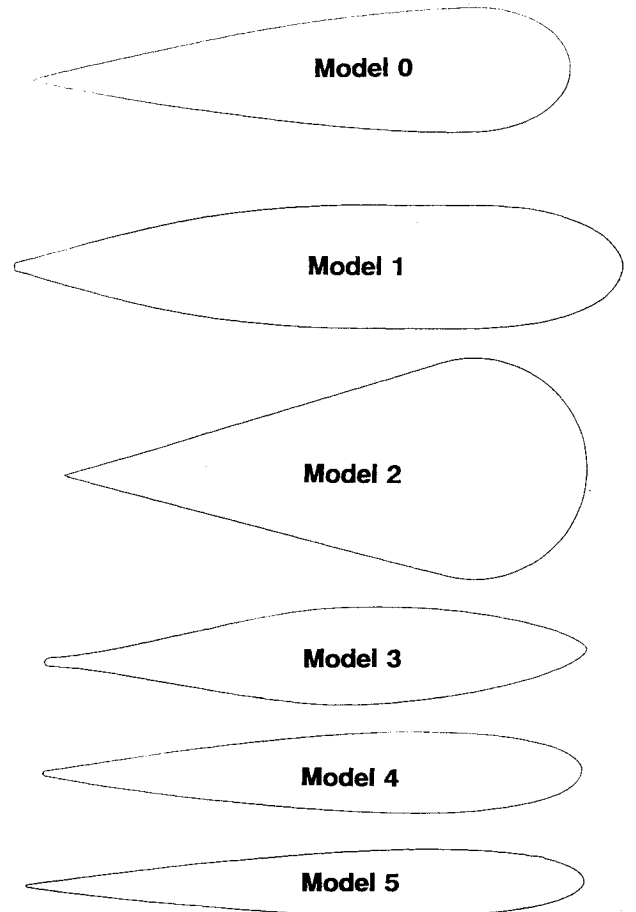

Fig. 2 Models used in the current investigation. Figure does not reflect the relative sizes. For important characteristics of the models, see Table 1.

Fig. 1 Schematic figure of the wing/body junction showing the microphone placement.

Table 1 Important characteristics of the models used

Model name	Model no.	Chord length, cm	Maximum thickness, cm	Axial location of maximum thickness location/c	Leading-edge radius/t	Maximum velocity location/c[a]	Trip location/c (circumferentially)	Trip length/c
3:2 Elliptical nose, NACA 0020 tail	0	30.48	7.17	0.1983	0.333	0.1262	0.1406	0.0208
Parallel centerbody model	1	44.22	8.89	0.3559	0.127	0.1423	0.158	0.0216
Tear drop	2	29.85	12.7	0.2156	0.5	0.1907	0.2542	0.0374
Sand 1850	3	61.04	11	0.4256	0.0497	0.4256	0.1372	0.0375
NACA-0015	4	60.81	9.21	0.3036	0.164	0.1327	0.1152	0.0376
NACA-0012	5	40.64	4.9	0.3079	0.131	0.1198	0.0918	0.0375

[a]Fleming.[2]

with a diameter of 12.7 cm, the tail of the body after $x/c = 0.235$ was made with planar surfaces. The shapes of the parallel centerbody model and Sand 1850 are given in Ref. 6.

C. Experimental Techniques

The measurement techniques employed in the present investigation include hot-wire anemometry, microphones for pressure-fluctuation measurements, and oil-flow visualization.

Within the next paragraphs, the instrumentation used for each technique, the reduction equations for the data, and information extracted from each technique will be discussed.

1. Oil-Flow Visualization Technique

The oil-flow visualization technique was used to extract information about the limiting streamline structure on the floor on which each wing is mounted. With this method the separation, reattachment of the flow, the line of low shear where the flow generates low shear, and wake region of the wings could be detected. The technique uses a mixture of TiO_2, kerosene, oleic acid in 20:50:9 ml ratio, respectively. First, a glossy black self-adhesive sheet (Frisk Coverseal) was laid on top of the surface where the visualization was done. Next, the mixture was applied with a brush such that the strokes of the brush were perpendicular to the main flow direction. Then the tunnel was run for 15–20 min and the mixture was left to dry. Later, the sheet was peeled off, further dried, and sprayed with lacquer fixer to preserve and permit photocopying.

2. Pressure-Fluctuation Technique

Pressure-fluctuation measurements were carried out using two Sennheiser MKH 110 microphones and Hewlett-Packard (HP 6213) power supply. The data were taken with a sampling rate of 10 kHz using a universal wave form analyzer DATA 6000 (Model 611 Data Precision Corporation, Analogic Corporation). Simultaneously taken data from the microphones were stored in an IBM PC-AT through a GPIB cable with the use of a TECMAR INC. A/D board. Thirty loads of data taken each with 16,384 consecutive measurement points resulted in 491,520 data points for each of the microphones in 49.152 s. The data are stored on an optical disk (Panasonic 940). The reduction of the data was carried out in an IBM PC-RT and the results are again saved to optical disks. The raw data after reduction yielded the p_{rms}/q_{ref}, the histograms of the data, skewness, flatness of these histograms, and the power spectra.

The measurements with the microphones were taken at the upstream of the leading edge of the wing on the floor along the stagnation line (Fig. 1). Two microphones each in their own circular casing were held together by an aluminum piece. The microphones were mounted from under the tunnel through a larger hole in an aluminum insert plate. The microphone casings were made flush to the tunnel floor and the gap between each casing and the floor was covered with Scotch tape.

Each casing had five holes each 0.75 mm in diameter along a diameter of the casing and ≈ 2.1 mm apart from each other along the centerline of the circular casing. During the measurements always only one hole on each microphone casing was left open to increase spatial resolution of the microphones. The microphone casings were made out of Plexiglass.

The frequency-response calibration of the microphones for such a casing and microphone combination was carried out by Simpson et al.[7, 8] They used a Genrad Model 1956 sound-level calibrator between 125 Hz–4 kHz and 74–114 dB SPL. The sensitivity of the combination is 20 mV/Pa for low frequencies but decreases above 1.5 kHz with the reduced frequency response.[7]

The p_{rms}/q_{ref} was obtained by using the power spectrum of the data corrected to take into account the frequency dependence of the sensitivity of the microphones. Histograms formed from the voltage data give information about the bimodality

of the data. Skewness and flatness indicated the variation of the histogram from Gaussian random distribution of the fluctuations.

The reduction of the data to obtain the power spectrum was made with the technique developed by Agarwal and Simpson.[9] Time-dependent pressure fluctuation $p(t)$ can be assumed to consist of

$$p(t) = p_t(t) + p_v(t) + p_a(t) \tag{1}$$

where t = turbulent, v = vibrational, and a = acoustic contributions, respectively. In that study, simultaneously time-series data from two adjacent microphones were used to find the turbulent pressure fluctuation in a two-dimensional flow. The procedure depends on the assumption that if the time-series data obtained from one microphone are delayed by τ s and subtracted from the other microphone data, then the coherent acoustic and the coherent vibrational components of the pressure fluctuations cancel each other for the specific frequency $f = 1/\tau$ and higher harmonics. For the same frequency and higher harmonics, the turbulence-produced pressure fluctuations are uncorrelated for time delays of $\tau > \delta/U_c$ because turbulence is not coherent over relatively long time delays. Here δ is the shear-layer thickness and U_c is the wave speed of the turbulent pressure fluctuations at that frequency. In the present study, the same procedure was applied to the data obtained from a single microphone. 4096 data points of each record were shifted by 1024 points. The time-delayed signal was subtracted from the undelayed signal at overlapping 2048 points. τ was selected to be quite long since neither the shear-layer thickness nor the U_c wave speed for the flow ahead of any of the wing was readily available. This in turn helped the frequency f to be quite small. Frequency f was chosen as 10,000/2048 which corresponded to a time delay of $\tau = 0.1024$ s which is ≈ 20 times bigger than the maximum delay applied in that paper. The power spectrum was calculated by using a Fast Fourier Transform program.[10] The power spectra were corrected with the calibration transfer function. By selecting τ high and f small resulted in only one time-delay value being sufficient for the whole frequency domain, since the equations written are also valid for the higher harmonics of the $f = 1/\tau$ frequency.

3. Histogram Calculation

The histograms of the pressure-fluctuation data were computed by dividing the -5.126 V to 5.126 V sampling range of the DATA 6000 into 2048 bins; being converted to pressure fluctuations using 20 mV = 1 Pa, and finding the number of samples falling into each bin. The probability density function of the whole 30 loads for each measurement location was computed by summing individual probability density function and equating the area underneath to be 1.

The flatness and skewness of the points were computed using the probability density functions and

$$\text{Skewness} = \overline{p^3} / (\overline{p^2})^{3/2}, \qquad \text{Flatness} = \overline{p^4} / (\overline{p^2})^2 \tag{2}$$

D. Uncertainty Analysis

Uncertainty in p_{rms}/q_{ref} was calculated using the analysis described in Bendat and Piersol.[10] The normalized bias error and random error in $\overline{p^2}$ are computed using

$$\left(\frac{\delta\overline{p^2}}{\overline{p^2}}\right)_{random} = \frac{\epsilon_r\sqrt{\Sigma\phi^2(\omega)(\Delta\omega)^2}}{\Sigma\phi(\omega)\Delta\omega}, \qquad \left(\frac{\delta\overline{p^2}}{\overline{p^2}}\right)_{bias} = \frac{\Sigma\epsilon_b\phi(\omega)\Delta\omega}{\Sigma\phi(\omega)\Delta\omega} \tag{3}$$

as 1.64% and 8.6%, respectively, where

$$\epsilon_b = B_e^2\phi(\omega)''/24\phi(\omega), \qquad \epsilon_r = 1/\sqrt{B_e T} \tag{4}$$

ϵ_b stands for the normalized bias error, ϵ_r denotes the random error for a given bin of the spectrum, B_e is spectrum analysis

bandwidth, T is the total record time, $\phi(\omega)$ is the autospectral density function, and $\phi(\omega)''$ is the second derivative with respect to ω. In the time-delayed analysis, half of the 491,520 points sampled with 10 kHz were used. This results in $T = 24.576$ s and $B_e = 4.88$ Hz. Second derivatives were computed by using a second-order central differencing scheme.

Uncertainties in skewness and flatness were found by using the definition equations of these quantities and the analysis described in Kline and McClintock.[11] The equations for the normalized uncertainty in skewness and the flatness are derived as

$$\Delta\text{Skewness/Skewness} = [9/4\,(\Delta\overline{p^2}/\overline{p^2})^2 + (\Delta\overline{p^3}/\overline{p^3})^2]^{1/2} \quad (5)$$

$$\Delta\text{Flatness/Flatness} = [4\,(\Delta\overline{p^2}/\overline{p^2})^2 + (\Delta\overline{p^4}/\overline{p^4})^2]^{1/2} \quad (6)$$

The uncertainty in $\overline{p^3}$ and $\overline{p^4}$ were not known and are estimated to be $\pm 15\%$ and $\pm 20\%$, respectively. This results in a $\pm 21\%$ uncertainty for skewness and a $\pm 28\%$ uncertainty for flatness.

Uncertainty in the oil-flow visualizations is expected to occur only due to the uncertainty in the length readings. The readings were made from the original pictures using a caliper but the oil accumulated in a wider band than a line. The uncertainty is expected to be within ± 2 mm.

III. Experimental Results

A. Oil-Flow Visualization Results

The oil-flow visualization pictures are presented in Figs. 3–8. Figures show that these oil-flow visualizations have similar characteristic features. The flow ahead of a wing separates because of an adverse pressure gradient due to the presence of the wing and forms the primary separation line[12] that passed through a stagnation point along the line of symmetry. The vortex formed downstream of this separation wraps itself around the wing to form the horseshoe vortex. A line of low
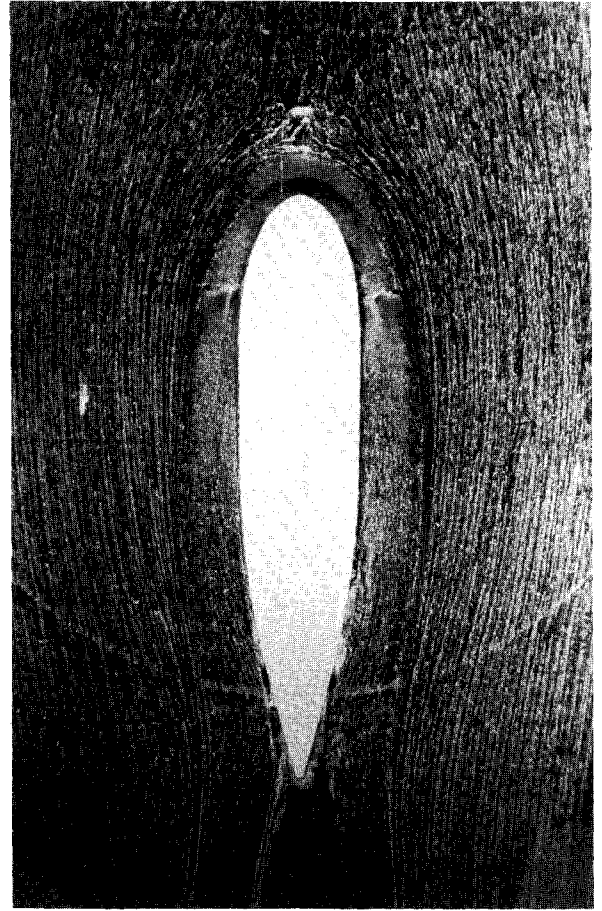

Fig. 4 Oil-flow visualization picture obtained for model 1 (parallel centerbody model).
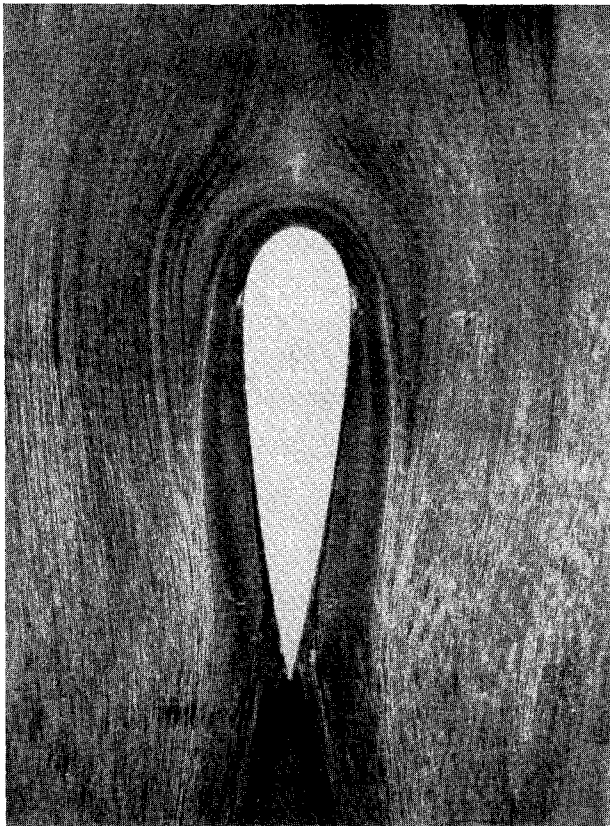

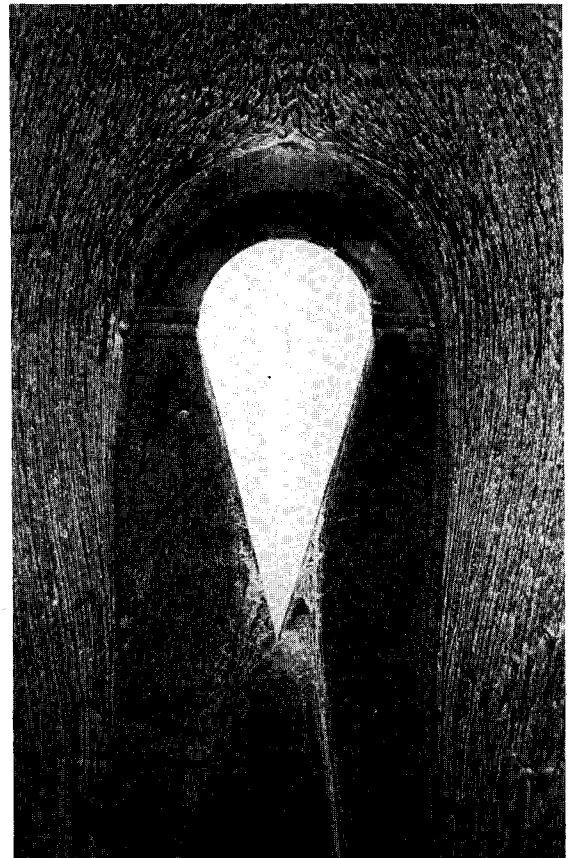Fig. 3 Oil-flow visualization picture obtained for model 0 (3:2 elliptical nose, NACA-0020 tail).

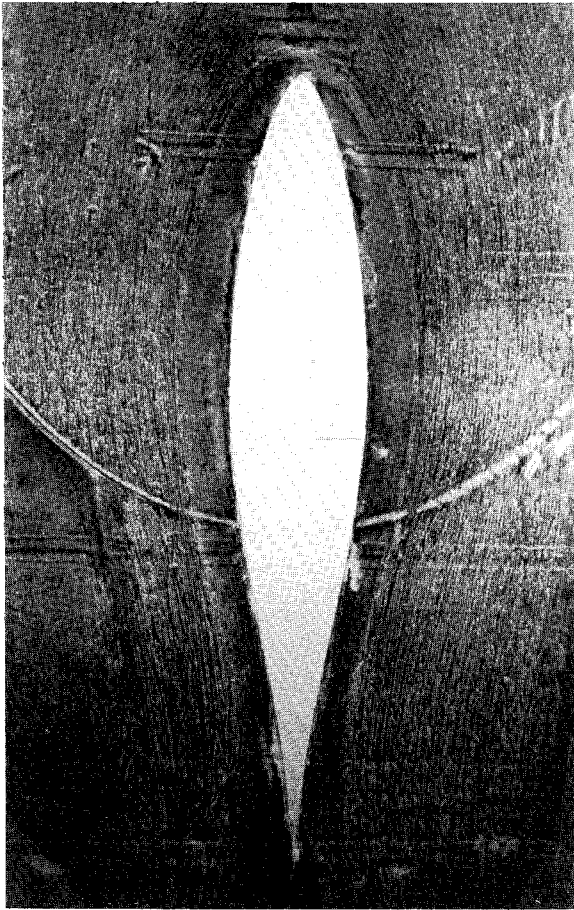Fig. 5 Oil-flow visualization picture obtained for model 2 (tear drop body).

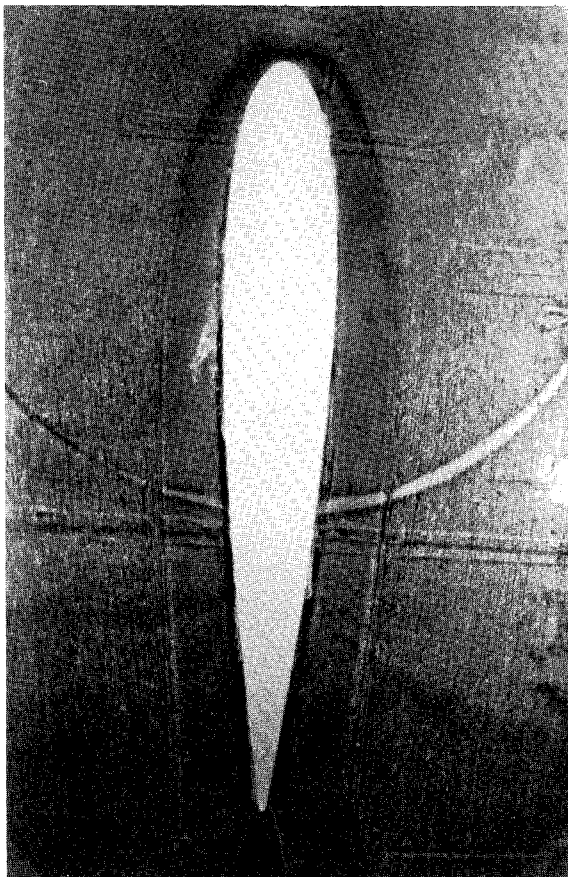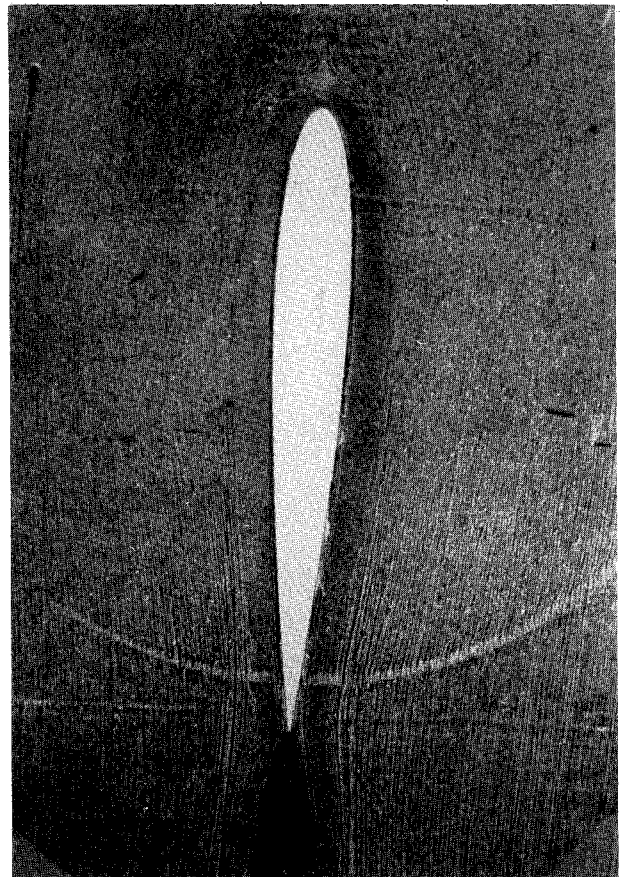Fig. 6   Oil-flow visualization picture obtained for model 3 (Sand 1850).

shear, along which the skin friction is relatively low is an open separation[12] line, is also observed between the primary separation line and the wing for each model. The primary separation line and the line of low shear merge with each other downstream. Further downstream, the flow close to the wall separates from the wing to form the fish-tailed wake region. From the figures, the width of the wake region and the maximum width of the area where the horseshoe vortex is confined could be measured. Some important characteristic lengths observed in the oil flows are shown schematically in Fig. 9. All of the characteristic dimensions nondimensionalized with the maximum thickness of each wing can be found in Table 2.

The models were tested at 0-deg angle-of-attack (AOA) of the wing. The AOA in turn was found by the oil-flow visualization pictures. Therefore to be able to ensure that the models were kept at 0-deg AOA, several trial runs were made.

Among the models tested, model 2 (tear drop) was observed to cause the most unsteady flowfield in the wake. Small changes in AOA could cause the flow on the wing to separate much earlier on one side than the other.
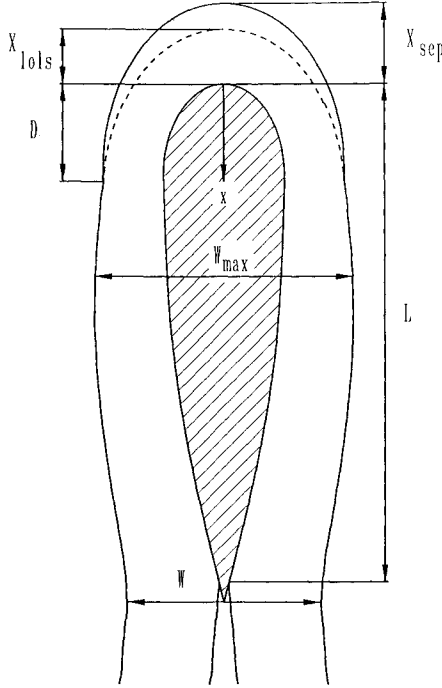
B.   Pressure-Fluctuation Measurement Results

Pressure-measurement results consist of power spectra which are used to compute the p_{rms}, histograms of the acquired voltages, and skewness and flatness computed from these histograms. The pressure fluctuations and the calculated skewness and flatness are presented in Figs. 10–12, respectively.

The p_{rms}/q_{ref} profiles near the nose start with values in between 0.04 to 0.06 which are well above the most upstream average value of $p_{rms}/q_{ref} \approx 0.0115$. At this region, while the skewness values are in the range of 0.25–0.5, flatness values are close to 3. In the vicinity of the line of low shear, p_{rms}/q_{ref} profiles form a peak and gradually decrease at the further upstream locations (Table 3). At the peak location of the p_{rms}/q_{ref} profiles, flatness profiles form a minimum, and fur-
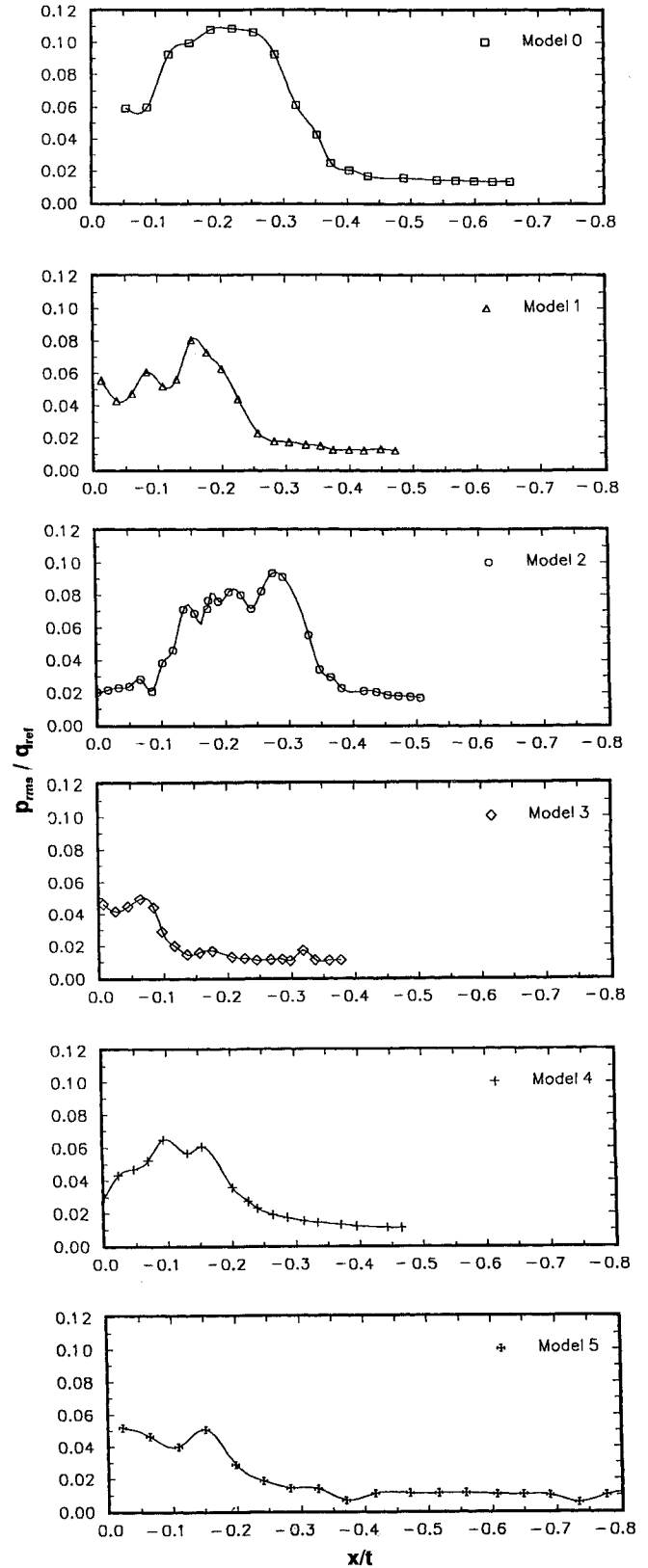

Fig. 7   Oil-flow visualization picture obtained for model 4 (NACA-0015).

Fig. 8   Oil-flow visualization picture obtained for model 5 (NACA-0012).

Table 2 Characteristic lengths measured from the oil-flow visualization pictures[a]

Model name and no.	X_{sep}	X_{lols}	D	L	W	W_{max}
Model 0	−0.45	−0.27	1.38	3.76	1.72	2.02
Model 1	−0.393	−0.194	0.756	4.573	1.565	2.056
Model 2	−0.518	−0.276	0.547	1.585	1.893	1.934
Model 3	−0.157	−0.067	1.620	4.212	0.810	1.743
Model 4	−0.294	−0.156	0.999	6.345	1.399	1.993
Model 5	−0.339	−0.146	1.953	7.598	1.366	1.985

[a]Lengths are normalized with t

Fig. 9 Definition of the characteristic lengths measured from oil-flow visualization pictures.

Fig. 10 Pressure fluctuations computed for the models. Note that t changes with the body shapes.

ther upstream before the low value skirts of p_{rms}/q_{ref} profiles are defined, they form a maximum. The latter points are also seen to be the locations where the skewness profiles form a minimum, below 0. The change in the sign of skewness values from positive to negative and again back to positive occurs between the line of low shear location and the first separation line. At further upstream locations, skewness values are seen to be between 0.25–0.3 and flatness values close to 3.5. Overall the skewness values were seen to gather on the positive side and the flatness values were different than 3, which shows that most of the histograms obtained were not Gaussian.

Bimodal histograms were obtained for model 0, 1, 2, and 4. For brevity, only results for model 0 are presented here in Fig. 13. The bimodal histograms occur in the range $x/t \approx -0.12$ to -0.319. Upstream and downstream of this flow region the pressure fluctuations occur in only one mode of the histogram. This bimodal region corresponds to the bimodal flow-field of the velocity fluctuations measured between $x/t \approx -0.11$ to -0.38, using the same model and the same tunnel, although the incoming boundary layer was thicker in that investigation.[3] The bimodal zone in model 1 is seen to be confined to $-0.153 \geq x/t \geq -0.226$ region; a clear bimodal histogram is seen at $x/t = -0.153$ location. The other histograms show signs of bimodality, but the second peak in these histograms is not visible. Model 2, the tear drop body, is seen to be having the widest range of the bimodal histogram zone. The zone spans in $-0.135 \geq x/t \geq -0.332$. Model 4 results in a bimodal histogram only at a point at x/t

$= -0.178$. Even though the peaks of the histogram are not distinct, the histogram shows two distinct zones around which the data tend to gather.

From Tables 1 and 2, it can be seen that the locations of the line of low shear point ahead of the nose, the locations where maximum p_{rms} was obtained and the locations where the flatness profiles reach to their minimum are seen to be in close proximity to each other and this point was also observed to be
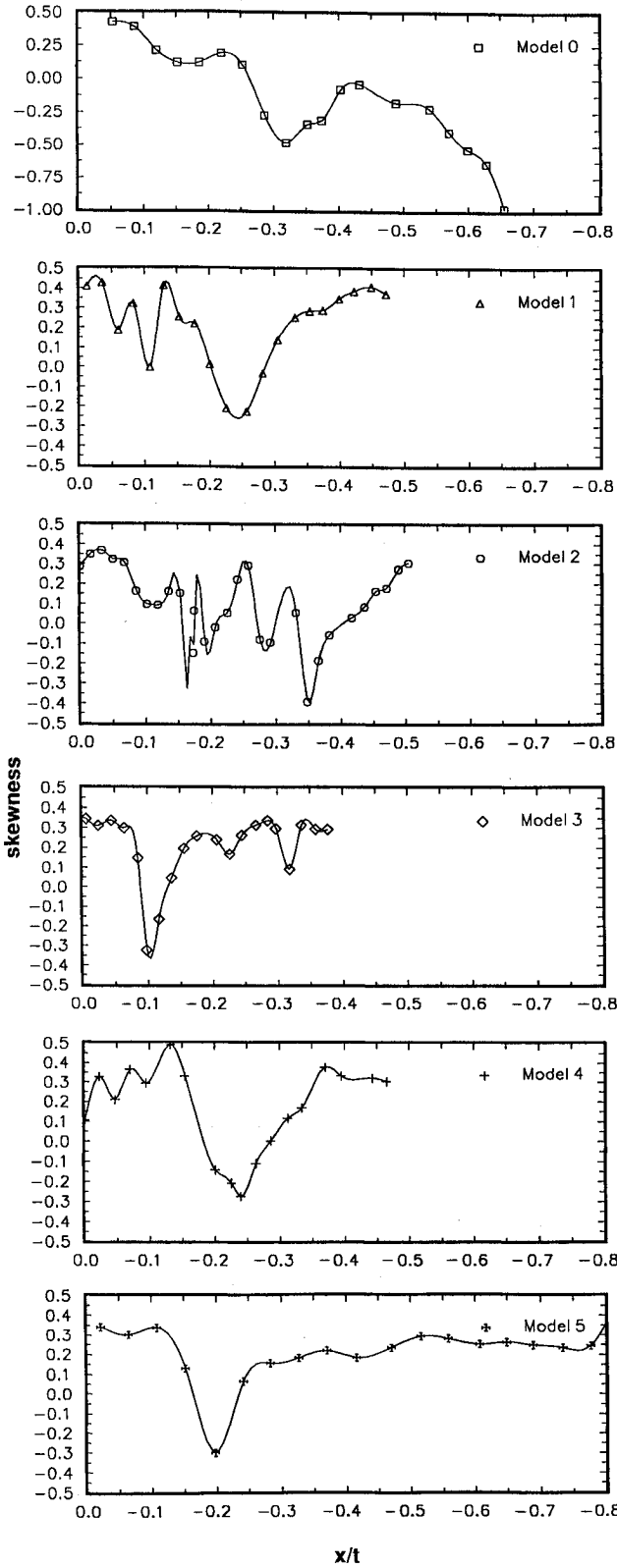
Fig. 11 Skewness values computed for the models. Note that t changes with the body shapes.
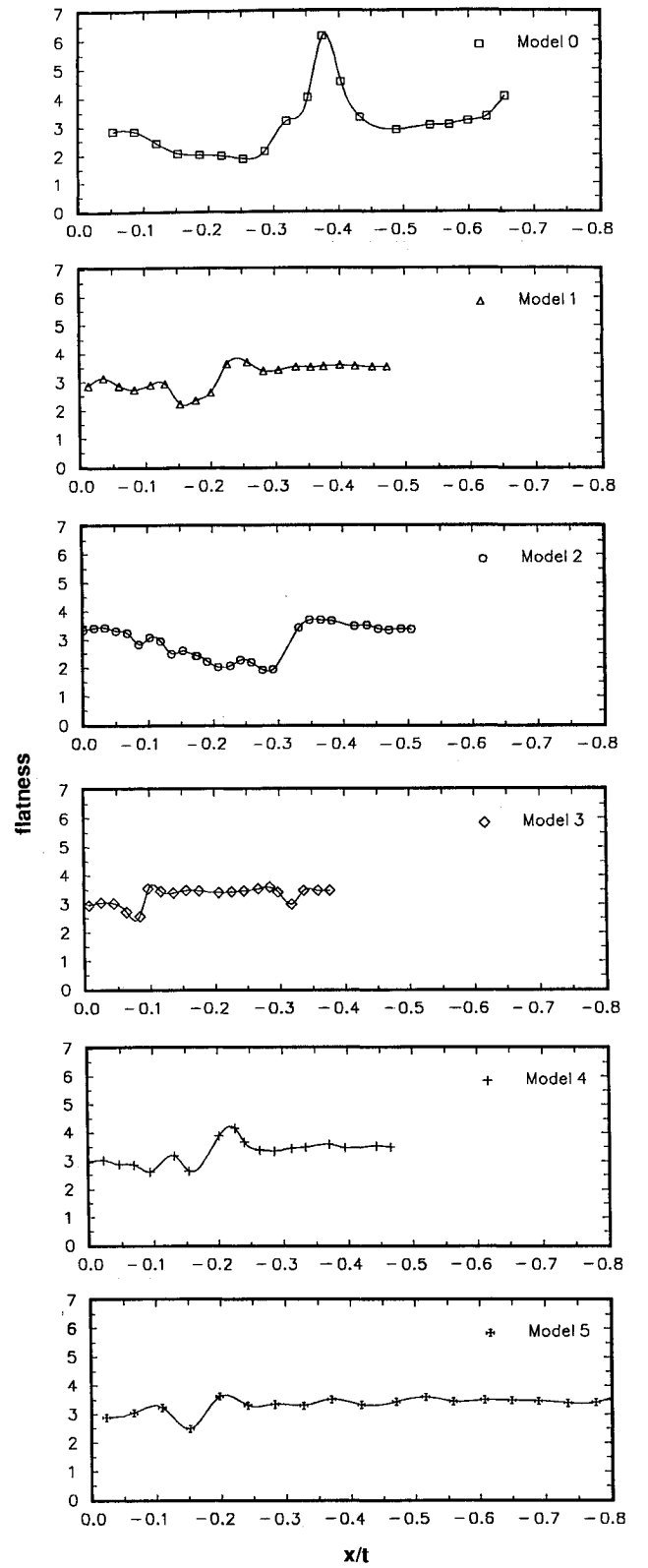
Fig. 12 Flatness values computed for the models. Note that t changes with the body shapes.

in close proximity to the center of the bimodal region (where the pressure fluctuations are equally distributed around the two peaks) at least for the models 0 and 2 which have clearer and longer bimodal histogram regions.

The spectra of the data of model 0 are presented in Fig. 14. For the computed spectra, the data above $\omega\delta^*/U_{ref} \approx 0.88$ are not reliable because the microphone frequency response is low. Figure 14 also shows lines with slopes -0.7, -1.0, and

-5.0. For all of the spectra including for all of the other models, regions with these slopes could not be observed. For model 0, the spectral value is seen to increase for $\omega\delta^*/U_{ref}$ below 0.3 until the bimodal zone is reached, with higher increments for $\omega\delta^*/U_{ref}$ less than 0.02. For the other models' spectra, even though the spectral values increase when the bimodal region is reached, the spectra were seen to form a peak between $\omega\delta^*/U_{ref} \approx 0.02$–0.03. The noise and acoustical

Table 3 Locations and minimum and maximum values of p_{max}, skewness, and flatness

Model no.	Maximum p_{rms} location and value		Minimum skewness location and value		Minimum and maximum flatness values and locations			
	x/t	p_{rms}/q_{ref}	x/t	Skewness	x/t	Minimum flatness	x/t	Maximum flatness
Model 0	−0.2194	0.1087	−0.319	−0.481	−0.25	1.856	−0.374	6.1377
Model 1	−0.1769	0.0807	−0.257	−0.224	−0.153	2.219	−0.257	3.688
Model 2	−0.276	0.0933	−0.348	−0.391	−0.276	1.925	−0.348	3.7
Model 3	−0.0639	0.0493	−0.098	−0.324	−0.0845	2.572	−0.0979	3.351
Model 4	−0.0943	0.0648	−0.239	−0.274	−0.0943	2.619	−0.201	3.872
Model 5	−0.1517	0.0506	−0.198	−0.298	−0.152	2.485	−0.198	3.622
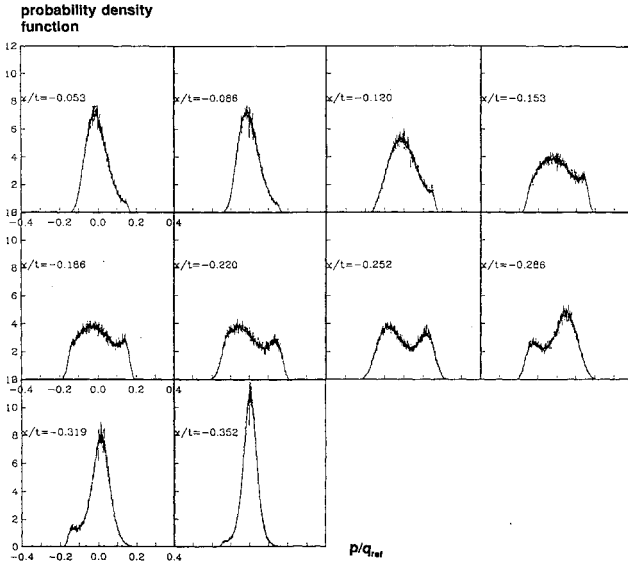
Fig. 13 Some of the probability density functions calculated for model 0.

Fig. 14 Power spectra calculated for model 0.

effect at low frequencies were eliminated by the data-reduction method described above.

C. Simple Physical Relationship Between the p_{rms} and the Body Geometry

A relation between the body geometry and the p_{rms} was found with the argument that the ratios of the force generated by the pressure fluctuations on the flat-body surface to the longitudinal and vertical momentum flow rate of the incoming fluid near the nose should be related to each other and also to the body geometry. The flowfield at the nose region of the wing is highly affected by the wing geometry, since the wing geometry influences the mean pressure gradients on the flowfield and controls the stretching of the horseshoe vortices around the nose. These mean flow effects produce a self-induced unsteady flow. The resulting unsteady flowfield of a horseshoe vortex suggests that the pressure fluctuations are more likely to be caused by the unsteady character of the horseshoe vortex structure rather than the turbulent nature of the approaching boundary layer. Thus, mean flow variables are related to p_{rms} because the mean flow determines the self-induced unsteady flow. Figure 15 shows the lengths, areas, and angles used in the following equations.

With the assumption that the vortex forming at the nose of the body acts like an obstacle and only half X_{sep} length portion closer to the wing allows the vertical velocities towards the wall and the incoming fluid flows out of this control volume from the sides, a continuity equation can be written. Even though this contradicts the unsteady character of the vortex, from the oil-flow pictures it can be seen that over a long period of time the vortex is confined to a zone near the nose, between the leading edge of the wing and the separation line. The U
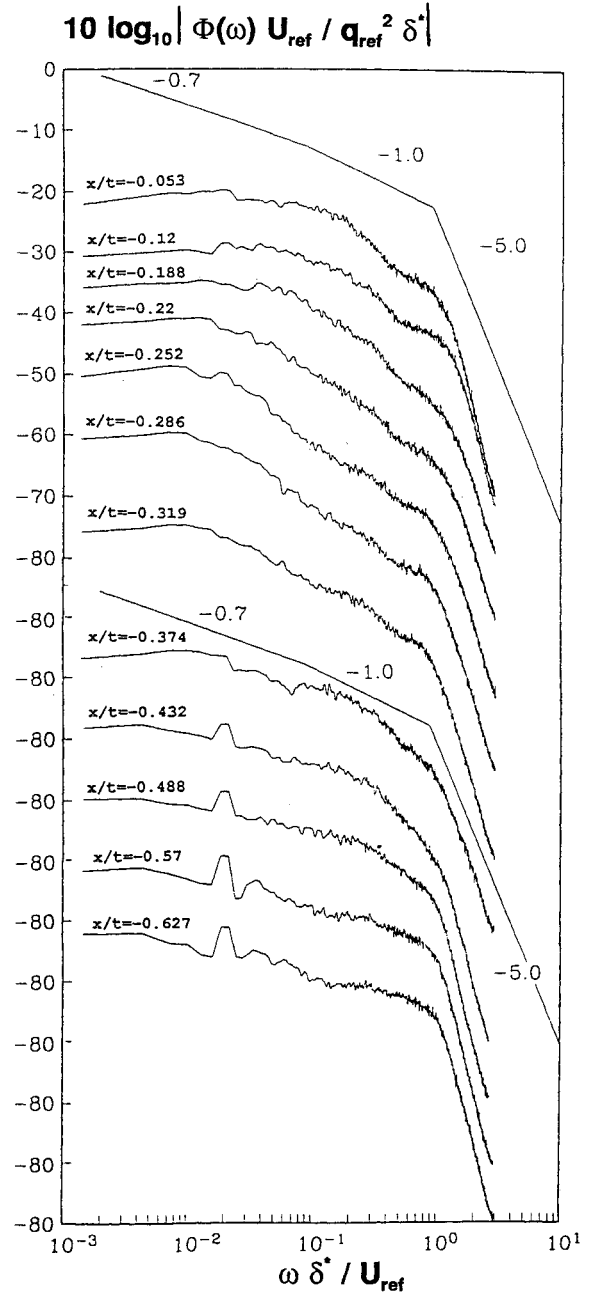
and V velocities are the average velocities at the entrance and exit of the control volume.

Continuity equation can be written as

$$\rho V \frac{\pi}{360}(90-\theta)\left[\left(R+\frac{X_{sep}}{2}\right)^2 - R^2\right] = \rho U\left(\frac{X_{sep}}{2}\delta + \frac{\pi}{8}\delta X_{sep}\right)$$

(7)

The momentum rate of the fluid coming in with the V velocity can be written as

$$V \text{ momentum} = \rho V^2 \text{ Area}_1 \qquad (8)$$

and the characteristic momentum rate effecting the vortex zone in the longitudinal direction may be written as

$$U \text{ momentum} = \rho U_{\text{ref}}^2 \delta X_{\text{sep}} \qquad (9)$$

The pressure fluctuations on the average generate a force as

$$\text{Pressure force} = \bar{p}_{\text{rms}} * \text{Area} \qquad (10)$$

where

$$\text{Area} = \frac{\pi}{360} (90 - \theta)(X_{\text{sep}}^2 + 2RX_{\text{sep}})$$

$$\text{Area}_1 = \frac{\pi}{360} (90 - \theta)(X_{\text{sep}}^2 + 2RX_{\text{sep}})$$

$$\text{Area} = \frac{\pi}{360} (90 - \theta)\left[\left(R + \frac{X_{\text{sep}}}{2} \right)^2 - R^2 \right]$$

$$\bar{p}_{\text{rms}} = \frac{\int_{x=0}^{x_1} p_{\text{rms}} \Delta x}{x_1}$$
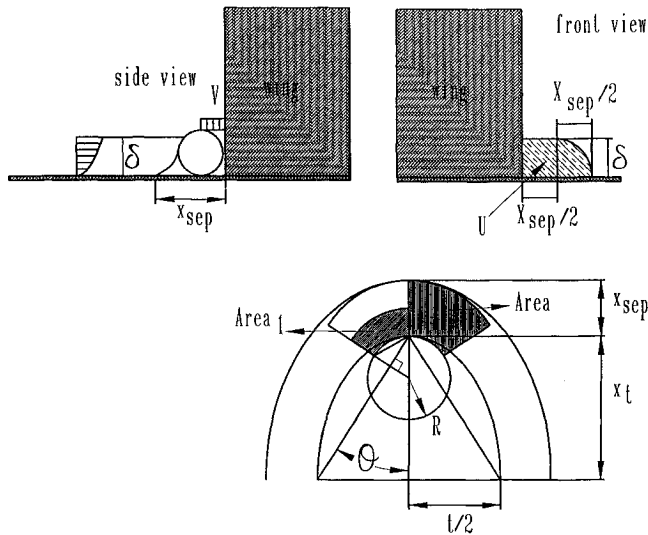
Fig. 15 Schematic showing geometric parameters used in the physical relationship between the pressure fluctuations and the wing geometry.
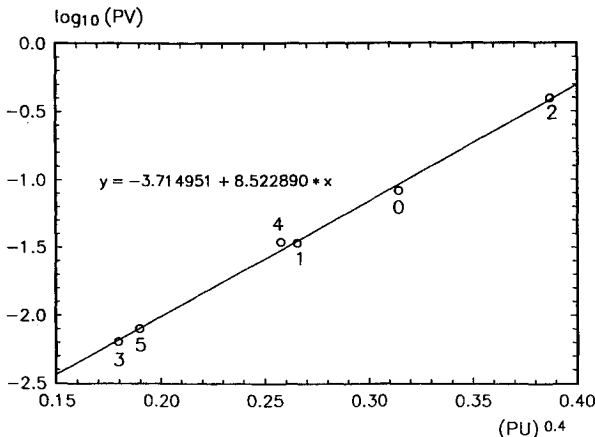
Fig. 16 A relation between the average pressure fluctuations and the wing geometry.

in the calculation of $\bar{p}_{\text{rms}}$ integration was stopped at the point x_1, where $p_{\text{rms}}/q_{\text{ref}}$ was lower than 0.0115. Extracting the V velocity in terms of U velocity from the continuity equation and replacing in the V momentum equation and assuming that the U velocity is related to the U_{ref} with $U = U_{\text{ref}}\cos\theta$ results in

$$PV = \frac{\text{pressure force}}{V \text{ momentum}} = \frac{2\pi^2 \bar{p}_{\text{rms}} (2R + X_{\text{sep}})(4R + X_{\text{sep}})(90 - \theta)^2}{q_{\text{ref}}(\cos\theta)^2\delta^2(4 + \pi)^2(180)^2}$$

$$(11)$$

$$PU = \frac{\text{pressure force}}{U \text{ momentum}} = \frac{\bar{p}_{\text{rms}}}{q_{\text{ref}}} \frac{\pi(90 - \theta)(X_{\text{sep}} + 2R)}{720\delta} \qquad (12)$$

ratios. Once (pressure force/U momentum rate) vs (pressure force/V momentum rate) was plotted, it was observed that a linear relation could be obtained as

$$\log_{10}(PV) = 8.5229 * (PU)^{4/10} - 3.71495 \qquad (13)$$

with a correlation coefficient of 0.998.

This relation can be seen in Fig. 16. Once the leading-edge radius, first separation length at the leading edge (X_{sep}), maximum thickness of the body, x_t maximum thickness location, incoming boundary-layer thickness, and undisturbed freestream velocity are known, $\bar{p}_{\text{rms}}$ could be computed iteratively.

IV. Conclusions

In this study, the nature of the pressure fluctuations at the nose section of a wing/body junction flow was investigated. For this purpose several different models were employed. Oil-flow visualizations were made to understand the limiting streamline structure on the wall. Data show that the line of low shear location is in close proximity of the locations where the flatness values are minimum and p_{rms} values are maximum and also close to the center of the bimodal regions for model 0 and 2. Overall, for the pressure-fluctuation data, the skewness was different than 0 and the flatness was different than 3 which shows that the distribution is not Gaussian. An empirical relation developed here shows that the average pressure fluctuation is logarithmically related to the V momentum rate and to the 0.4 power of the U momentum rate of the flow at the nose region.

Acknowledgments

References

[1]Mehta, R. D., "Effect of Wing Nose Shape on the Flow in a Wing/Body Junction," *Aeronautical Journal*, Vol. 88, Dec. 1984, pp. 456–460.

[2]Fleming, J., "An Experimental Study of Turbulent Wing-Body Junction and Wake Flow," M.S. Thesis, Dept. of Aerospace and Ocean Engineering, Virginia Polytechnic Inst. and State Univ., Blacksburg, VA, 1991.

[3]Devenport, W. J., and Simpson, R. L., "Time-Dependent and Time-Averaged Turbulence Structure Near the Nose of a Wing-Body Junction," *Journal of Fluid Mechanics*, Vol. 210, Jan. 1990, pp. 23–55.

[4]Kim, S. A., "Observation and Measurements of Flow Structures in the Stagnation Region of a Wing-Body Junction," Ph.D. Dissertation, Dept. of Aerospace and Ocean Engineering, Virginia Polytechnic Inst. and State Univ., Blacksburg, VA, 1991.

[5]Abbott, I. H., and von Doenhoff, A. E., *Theory of Wing Sections*, Dover Publications, New York, 1949, Chap. 6.

[6]Ölçmen, M. S., and Simpson, R. L., "Influence of Wing Shapes on the Surface Pressure Fluctuations of a Wing-Body Junction,"

AIAA Paper 92-0433, Jan. 1992.

[7]Simpson, R. L., Ghodbane, M., and McGrath, B. E., "An Experimental Study of Surface Pressure Fluctuations in a Separating Turbulent Boundary Layer," NASA CR-178309, June 1987.

[8]Simpson, R. L., Ghodbane, M., and McGrath, B. E., "Surface Pressure Fluctuations in a Separating Turbulent Boundary Layer," *Journal of Fluid Mechanics,* Vol. 177, No. 1, 1987, pp. 167–186.
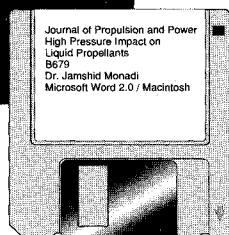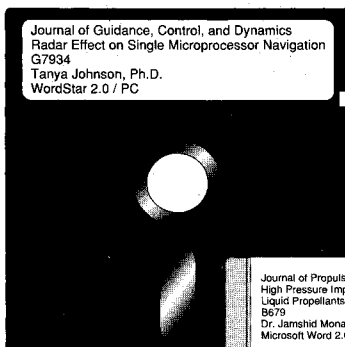
[9]Agarwal, N. K., and Simpson, R. L., "A New Technique for Obtaining the Turbulent Pressure Spectrum from the Surface Pressure Spectrum," *Journal of Sound and Vibration,* Vol. 135, No. 2, 1989,

pp. 346–350.

[10]Bendat, J. S., and Piersol, A. G., *Random Data, Analysis and Measurement Procedure,* Wiley-Interscience, Wiley, New York, 1986, Chaps. 8, 11.

[11]Kline, S. J., and McClintock, F. A., "Describing Uncertainties in Single Sample Experiments," *Mechanical Engineering,* Vol. 75, Jan. 1953, pp. 3–8.

[12]Peake, D., and Tobak, M., "Topology of Three-Dimensional Separated Flows," *Annual Review of Fluid Mechanics,* Vol. 14, 1982, pp. 61–85.